

This is the Name of my Thesis

by

I. B. Scriptor

B.A., North Dakota State University, 2005

M.S., University of Reno, 2007

A thesis submitted to the
Faculty of the Graduate School of the
University of Colorado in partial fulfillment
of the requirements for the degree of
Doctor of Philosophy
Department of Rocket Science
2017

This thesis entitled:
This is the Name of my Thesis
written by I. B. Scriptor
has been approved for the Department of Rocket Science

Prof. Ed Visor

Prof. Rachel Goddard

Ms. Thora Nea

Date _____

The final copy of this thesis has been examined by the signatories, and we find that both the content and the form meet acceptable presentation standards of scholarly work in the above mentioned discipline.

Scriptor, I. B. (Ph.D., Rocket Science)

This is the Name of my Thesis

Thesis directed by Prof. Ed Visor

Often the abstract will be long enough to require more than one page, in which case the macro “\OnePageChapter” should *not* be used.

But this one isn’t, so it should.

Dedication

To all of the fluffy kitties.

Acknowledgements

Here's where you acknowledge folks who helped. But keep it short, i.e., no more than one page, as required by the Grad School Specifications.

Contents

Chapter

1	Experimental Setup	1
1.1	The Large Hadron Collider	1
1.2	The Compact Muon Solenoid Detector	2
1.2.1	The Tracker	4
1.2.2	The Electromagnetic Calorimeter	7
1.2.3	The Hadron Calorimeter	8
1.2.4	The Superconducting Magnet	10
1.2.5	The Muon System	11
1.2.6	The Trigger System	13
2	Object Reconstruction	16
2.1	The Particle Flow Algorithm	16
2.1.1	Iterative Tracking	16
2.1.2	Calorimeter Clustering	17
2.1.3	The Link Algorithm	18
2.1.4	Particle Identification	18
2.2	Vertex Reconstruction	19
2.3	Jet Reconstruction	19
2.4	Missing Transverse Energy	20

3	Radiation Tolerance of 65 nm CMOS Transistors	21
3.1	Radiation Damage Mechanisms	22
3.2	Experimental Details	24
3.2.1	Transistor Test Setup	24
3.2.2	Irradiation Setup	25
3.3	Analysis	26
3.4	Results	28
3.5	Summary	29
Bibliography		34
Appendix		

Tables**Table**

3.1 The irradiation schedule, showing the 2 weeks it took to accumulate 1 Grad. 27

Figures

Figure

1.1	A schematic of the accelerator chain.	3
1.2	A sliced view of the CMS detector.	5
1.3	A schematic of the CMS tracker in the r-z plane.	5
1.4	A comparison of the 2016 pixel detector geometry with the 2017 upgrade geometry..	6
1.5	Schematic view of a quadrant of the electromagnetic calorimeter (ECAL). The numbers correspond to η and show the coverage of the different sections of the ECAL. .	9
1.6	Schematic cross section of the hadron calorimeter (HCAL).	9
1.7	Schematic view of the muon system.	12
1.8	Schematic of the Level-1 trigger system.	14
3.1	The cross section view of an n-channel transistor. The transistor is built on a p-type substrate with n-type implants as the source and drain. An inversion layer is formed in the conducting channel when a positive voltage is applied to the gate. The gate dielectric (gate oxide) and shallow trench isolation (STI) oxide are the green regions[16].	22
3.2	The crosses represent positive charge build up in the shallow trench isolation (STI) oxide, which allow current to pass between the source and the drain when no voltage is applied to the gate[11].	24

3.7 The change in maximum drain-source current for similar PMOS core transistors irradiated with different gate bias voltages. The graph on the left is for 120/60 transistors and the graph on the right is for 360/60 transistors. The lines connecting points do not represent a fit, and are included only to make the plots easier to read. The transistor characteristics measured for transistors in one of the test ASIC packages after 754 Mrad was accumulated were all offset by current not likely to have passed through the transistors (this can be seen in Figure 3.6). Lines are not drawn through these points. The most likely source of these offsets is leakage current due to moisture caused by condensation on the cold ASIC package.	31
3.8 Transistor characteristic curves during the annealing period for (left) a 120/60 core PMOS and (right) a 1000/280 2.5 V NMOS.	31
3.9 The graph on the left shows the loss of maximum drain-source current during irradiation for 4 PMOS core transistors. The graph on the right shows the recovery of maximum drain-source current for the same 4 transistors during and after annealing. As in Figure 3.11, lines are included to make the plots easier to read. Once again, lines are not drawn through the points corresponding to measurements made after 754 Mrad of transistors in one of the ASIC packages.	32
3.10 The graph on the left shows the loss in maximum drain-source current after each irradiation step for 9 NMOS core transistors. The graph on the right shows the change in maximum drain-source current for the same 9 transistors during and after annealing.	32
3.11 The shift in threshold voltage for 8 NMOS I/O transistors irradiated to 878 MRad is shown in the graph on the left, while the graph on the right shows V_{th} for the same 8 transistors during and after annealing. No significant annealing was observed for the two zero V_{th} I/O transistors.	33

Chapter 1

Experimental Setup

1.1 The Large Hadron Collider

The Large Hadron Collider (LHC) accelerates protons and heavy ions in counter rotating beams to near-light speeds. These beams are contained in vacuum tubes that form a circle 26.7 km in circumference and are housed between 50 and 175 m underground, near the France-Switzerland border. The beams cross at four interaction points where four different detectors are located.

In ideal conditions, each beam contains 2,808 bunches of protons and each bunch contains about 100 billion protons. These bunches are formed from the 16 radio-frequency (RF) cavities located on the beamline. The path and shape of the beam are controlled by about 9,600 magnets. Dipole magnets keep the beams on their circular path, while quadrupole magnets focus the beams. In order for the superconducting dipole magnets to provide a high magnetic field of 8.3 T, they must be kept at 1.9 K with superfluid Helium.

The design instantaneous luminosity, \mathcal{L} , is $10^{-34}\text{cm}^{-2}\text{s}^{-1}$ and only depends on beam parameters:

$$\mathcal{L} = \frac{N_b^2 n_b f_{rev} \gamma_r}{4\pi \varepsilon_n \beta} F \quad (1.1)$$

where N_b is the number of particles per bunch, n_b is the number of bunches per beam, f_{rev} is the frequency of the revolutions of the beam, γ_r is the relativistic factor, ε_n is the normalized transverse beam emittance, β is the beta function at the collision point and is roughly the width of the beam squared divided by the emittance, and F is the geometric luminosity reduction factor due to the

crossing angle at the interaction point [9]. Integrating the instantaneous luminosity with respect to time gives the integrated luminosity:

$$L = \int \mathcal{L}(t) dt \quad (1.2)$$

In 2016, the LHC provided 35.9 fb^{-1} of integrated luminosity and a similar amount is expected in 2017. This luminosity is delivered with a bunch spacing of 25 ns and a center of mass energy of 13 TeV. To achieve this, electrons are stripped off of Hydrogen atoms by an electric field and the remaining protons are injected into a linear accelerator (LINAC 2) where they reach an energy of 50 MeV. The beam is then sent to the Proton Synchrotron Booster (PSB), which accelerates the protons to 1.4 GeV. Afterwards, the beams are injected into the Proton Synchrotron (PS) where they reach 25 GeV, followed by the Super Proton Synchrotron (PSP) where they are accelerated to 450 GeV. The beams are then accelerated in the main ring to 6.5 TeV. A layout of the acceleration facility can be seen in Figure 1.1[13].

1.2 The Compact Muon Solenoid Detector

The Compact Muon Solenoid (CMS) detector is one of the general-purpose particle detectors at the LHC. It is made up of layered, sub-detectors arranged in a cylindrical structure that is 21.6 m long, 15 m in diameter and weighs about 14,000 tons. The detector is built around its huge solenoid magnet which provides a 3.8 T magnetic field. Due to the size of this magnet, the silicon tracker, the lead tungstate crystal electromagnetic calorimeter (ECAL), and the brass and plastic scintillator hadron calorimeter (HCAL) are all able to fit within the solenoid, allowing the momentum of particles to be precisely measured. Encasing the solenoid is the muon detector system composed of different types of gas-ionization detectors. A layout of the CMS detector can be seen in Figure 1.2.

The experiment uses a right-handed, Cartesian coordinate system that is oriented with the x-axis pointing to the center of the LHC ring, the y-axis pointing up, and the z-axis pointing along the beam line. A pseudo-polar coordinate system is also used due to the cylindrical symmetry of the

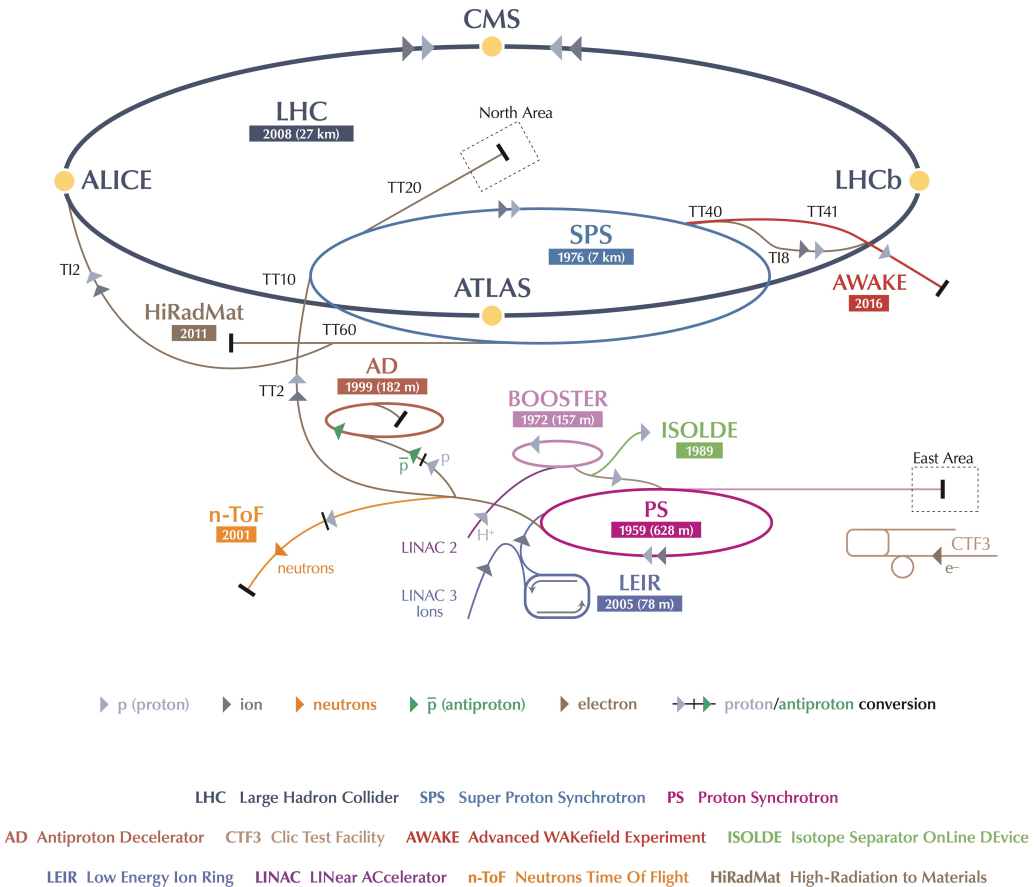


Figure 1.1: A schematic of the accelerator chain.

detector. The azimuthal angle, ϕ , is measured from the x-axis in the x-y plane, the polar angle, θ , is defined from the z-axis, and the pseudorapidity, η , is given by $\eta = -\ln \tan(\theta/2)$. The transverse plane is used to define the component of observable quantities, like momentum and energy, that is perpendicular to the beamline in the x-y plane.

1.2.1 The Tracker

The tracker is the innermost layer of the CMS detector and is completely made of silicon. It consists of 2 separate subdetectors: the inner pixel detector and the outer strip detector. The purpose of the tracker is to collect precise, three-dimensional single hit positions along the curved trajectories of charged particles to extract their momentum. The tracker covers up to a pseudorapidity of $|\eta| < 2.5$. A schematic of the tracker can be seen in Figure 1.3 [5].

1.2.1.1 The Pixel Detector

The pixel detector contains 65 million pixels that are $100 \times 150 \mu\text{m}^2$ with a thickness of $285 \mu\text{m}$. These pixels are contained in two different sections: the barrel (BPIX) and the endcaps (FPIX). The barrel is a cylindrical structure that surrounds the interaction vertex and consists of three concentric layers. These layers are at distances of 4.4, 7.3, and 10.2 cm from the beamlines. The endcap section consists of 2 symmetrical disk sections on either end of the barrel. Each section is made up of 2 disks that are 34.5 and 46.5 cm from the interaction point. At the end of the 2016 data taking period, an additional layer was added to the barrel region and the layers are now at distances of 3.0, 6.8, 10.2, and 16.0 cm. An additional disk was also added to each endcap region and each disk now consists of 2 concentric rings, inner and outer, to enable easy replacement. A comparison of the 2016 and 2017 pixel detector geometries can be seen in Figure 1.4[7].

The silicon pixels are grouped in modules of 52×80 pixels and bump-bonded to a read-out-chip (ROC). These ROCs amplify and shape the signals from the pixel sensors so that they can be converted from analog to digital signals.

Due to the proximity of the pixel detector to the interaction point, the sensors and readout

CMS DETECTOR

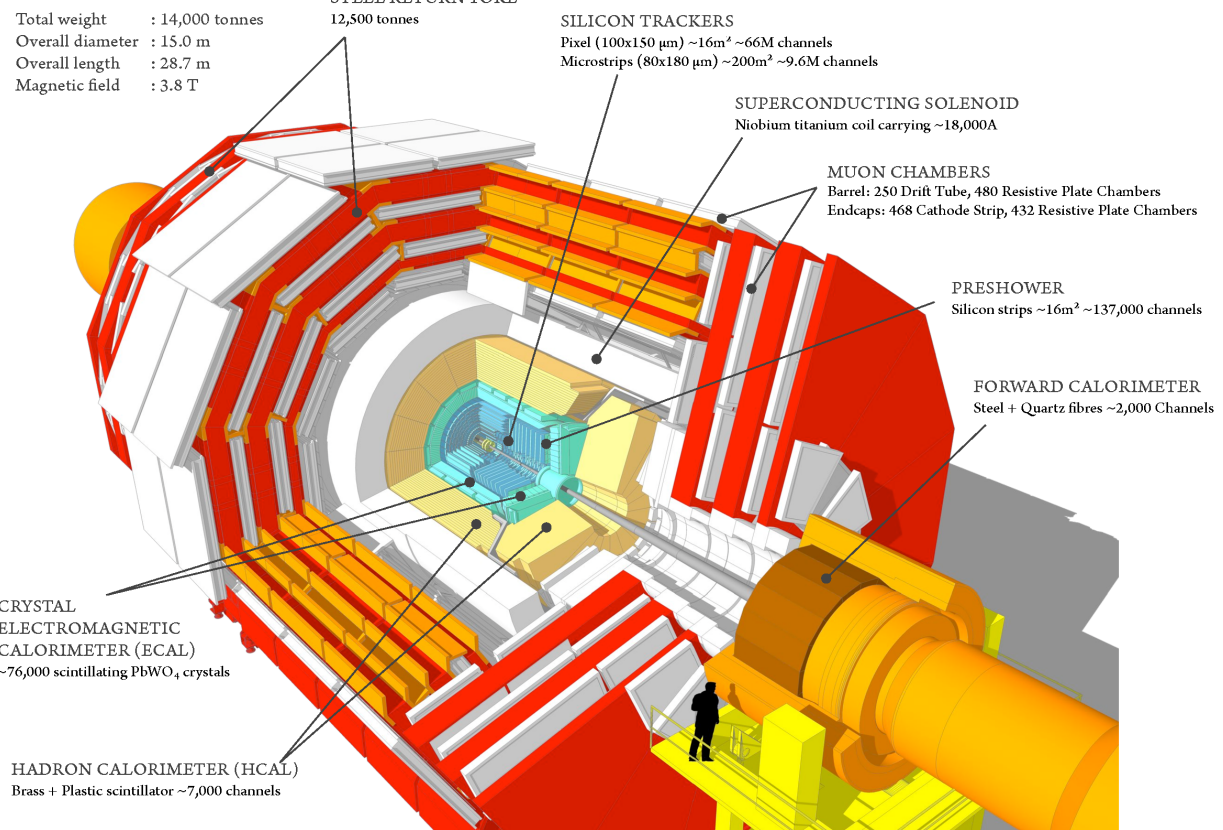


Figure 1.2: A sliced view of the CMS detector.

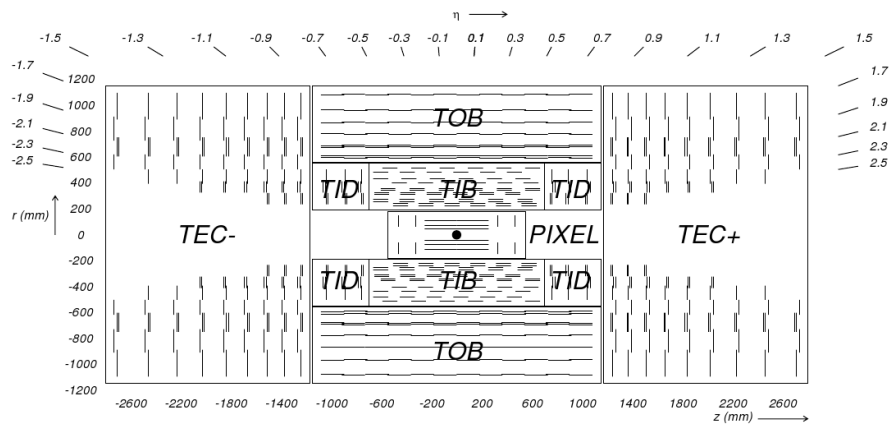


Figure 1.3: A schematic of the CMS tracker in the r-z plane.

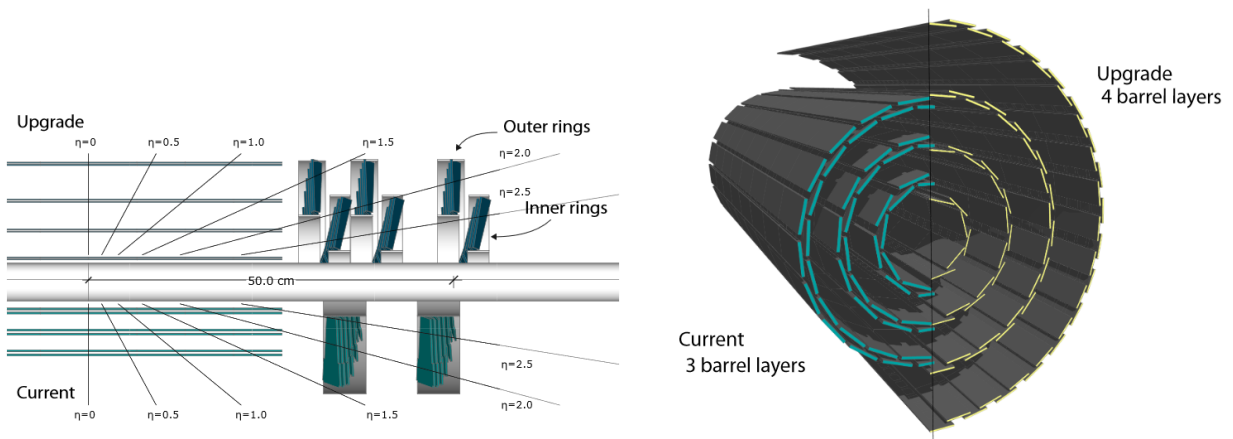


Figure 1.4: A comparison of the 2016 pixel detector geometry with the 2017 upgrade geometry.

electronics will receive an incredibly high particle flux. The innermost layer of the BPIX is expected to receive a radiation dose of 840 kGy after an integrated luminosity of 500 fb^{-1} . A radiation tolerant design was a top priority for both the electronics and sensors and more details on this will be given in Chapter ??.

1.2.1.2 The Strip Detector

Outside of the pixel detector is the strip detector which is arranged in a similar manner as the pixel detector. There is a barrel region that is split into an inner barrel (TIB) section and an outer barrel (TOB) section and two endcap sections on either side that consist of an inner endcap region (TID) and an outer endcap region (TEC). The TIB consists of four concentric cylinders that extend out to 65 cm on either side of the interaction point and have radii between 25.5 and 49.8 cm. The two inner layers are comprised of double sided modules with a strip pitch of $80 \mu\text{m}$ and the two outer layers are made of single sided modules with a strip pitch of $120 \mu\text{m}$. The TOB consists of 6 concentric cylinders that extend from -110 to $+110$ along the z axis and are between radii of 55.5 to 116.0 cm. Each TID consists of 3 disks located between $z = \pm 80 \text{ cm}$ and $z = \pm 90 \text{ cm}$. A disk consists of 3 rings which span radii from 20 to 50 cm. The 2 innnermost rings have double sided modules and the outermost has single sided ones. The TEC disks extend radially from 22 to 113.5 cm and are located between $\pm 124 \text{ cm}$ and $\pm 280 \text{ cm}$ along the z direction. The silicon sensors in the TIB, TID, and inner 4 rings of the TEC are $320 \mu\text{m}$ thick and the sensors in the TOB and 3 outer rings of the TEC are $500 \mu\text{m}$ thick[5].

1.2.2 The Electromagnetic Calorimeter

Surrounding the tracker is the electromagnetic calorimeter (ECAL) which measures the energies of electrons and photons. The ECAL is made up of lead tungstate (PbWO_4) crystals which produce scintillation light in fast, well defined photon showers whenever an electron or photon passes through them. These showers can be measured by photodetectors to determine the energy of the electron or photon. Since the yield of light in the crystals depends on temperature, the

temperature of the ECAL does not vary by more than 0.1°C .

The ECAL is made up of a barrel region which consists of 61,200 crystals and 2 endcap segments which consist of 7,324 crystals. The barrel covers a pseudorapidity of $|\eta| < 1.479$ and is made of crystals with a cross section of $22 \times 22 \text{ mm}^2$ and a length of 230 mm, which corresponds to 25.8 radiation lengths. The photodetectors in the barrel region are avalanche photodiodes and are made of silicon. The endcaps cover a pseudorapidity of $1.48 < |\eta| < 3.0$ and the crystals have dimensions $24.7 \times 24.7 \times 220 \text{ mm}^3$. The crystals are organized into groups of 36 crystals, called a supercrystal, and each endcap contains 268 supercrystals. The photodiodes in the endcaps are vacuum phototriodes and are used because of the higher radiation tolerance that is needed in this region.

Another component of the ECAL is the preshower detector. The preshower sits in front of both endcaps and covers a pseudorapidity of $1.65 < |\eta| < 2.61$. The purpose of the preshower is for extra spatial precision in order to distinguish single photons from a π^0 decaying to two nearby photons. The preshower is made of 2 planes of lead followed by silicon sensors that have dimensions of $6.3 \text{ cm} \times 6.3 \text{ cm} \times 0.3 \text{ mm}$ [5][4].

The layout of the ECAL can be seen in Figure 1.5.

1.2.3 The Hadron Calorimeter

The hadron calorimeter (HCAL) surrounds the ECAL and its purpose is to measure the energy of hadrons. It is designed to be a hermetic detector because all particles from an interaction must be detected to accurately measure the missing transverse energy (MET) of an event. The HCAL is a sampling detector that is made up of alternating layers of absorber and scintillator. The absorbers are made of either brass or steel and when a particle hits them a shower of particles is produced. Light is then emitted when particles pass through the scintillation material and absorbed by wavelength-shifting fibers that are less than 1 mm in diameter. The HCAL is divided into 4 sections: the barrel (HB), the endcap (HE), the outer calorimeter (HO), and the forward calorimeter (HF). A schematic of the HCAL can be viewed in Figure 1.6[5].

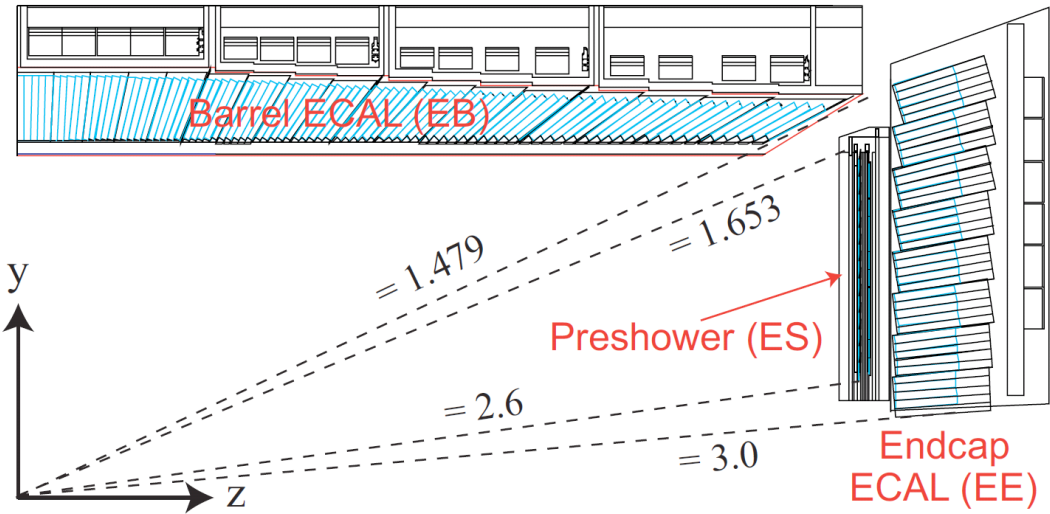


Figure 1.5: Schematic view of a quadrant of the electromagnetic calorimeter (ECAL). The numbers correspond to η and show the coverage of the different sections of the ECAL.



Figure 1.6: Schematic cross section of the hadron calorimeter (HCAL).

The HB sits inside the magnet and covers a pseudorapidity of $|\eta| < 1.3$. It is made up of 36 wedges aligned parallel to the beam axis, where each wedge consists of brass plates interspersed by plastic scintillator. The plastic scintillator plates are divided into 16 sections giving a granularity of $\Delta\eta \times \Delta\phi = 0.087 \times 0.087$. For structural support, the outermost layers of each wedge are steel plates.

The HE is designed to sustain a high radiation flux due to the pseudorapidity region it covers, $1.3 < |\eta| < 3$. It also must provide the maximum number of interaction lengths to contain hadronic showers. Thus, C26000 brass was chosen as the absorber and the combined material in the HE provides about ten interaction lengths. For $|\eta| < 1.6$ the granularity is $\Delta\eta \times \Delta\phi = 0.087^2$ while for $|\eta| \geq 1.6$ the granularity is $\Delta\eta \times \Delta\phi = 0.17^2$.

Due to the limited space within the solenoid magnet, the HO sits outside of the magnet and detects any late starting showers. The HO covers $|\eta| < 1.3$ and adds more material to the barrel region to provide 11.8 radiation lengths. Since the HO detects energy that would otherwise be missed, it improves missing transverse energy (MET) measurements.

The HF sits 11.2 m from the interaction point down the beam line. It is a cylindrical structure with an outer radius of 130 cm. Due to the extreme, 760 GeV energy per proton-proton interaction deposited into the forward calorimeters, quartz fibers are used as the active medium. It has a granularity of $\Delta\eta \times \Delta\phi = 0.175 \times 0.175$ and covers a pseudorapidity range of $3.0 < |\eta| < 5.0$.

1.2.4 The Superconducting Magnet

As implied by the name of CMS, the superconducting magnet is a central design feature of the detector. By producing a uniform, 3.8 T magnetic field the paths of charged particles are bent and the momentum of these particles can be accurately measured. The magnet is a solenoid with a length of 12.5 m and a 6.3 m inside diameter. This large space allows the tracker, ECAL and HCAL to fit inside the solenoid. The magnet is made up of 4-layers of NbTi wires that are coiled and then cooled to -268.5°C to allow electricity to flow through with minimal resistance and produce the largest magnetic field possible. The magnetic flux is returned through a yoke that weighs 10,000

tons and is made up of six endcap disks and five barrel wheels.

1.2.5 The Muon System

The muon system is the outermost sub-detector of CMS since muons have a small cross section and can pass through several meters of iron without interacting. There are 1400 muon chambers that compose the muon system and these chambers consist of three different types of detectors: drift tubes (DTs), cathode strip chambers (CSCs), and resistive plate chambers (RPCs). The muon system sits between the magnet return yolk and covers a pseudorapidity of $|\eta| < 2.4$. The DTs and RPCs make up the barrel region of the sub-detector and the CSCs and RPCs make up the endcap regions. A detailed view of the muon system can be seen in Figure 1.7[5].

The DTs are 4 cm wide tubes that contain a wire within a gas volume comprised of 85% Ar and 15% CO₂. The muons knock electrons off the atoms of the gas and collect on the wire where a positive voltage is applied. The drift velocity of electrons in the gaseous mixture is known and thus two position coordinates can be measured. The DTs are arranged in 4 concentric cylinders around the beamline and cover a pseudorapidity of $|\eta| < 1.2$.

CSCs are made of arrays of positively charged anode wires crossed with negatively charged cathode strips within a gas volume. Electrons from the interacting muons are detected in a similar way as the DTs and since the wires and strips are perpendicular to each other 2 position coordinates are measured. The CSCs cover the pseudorapidity range $0.9 < |\eta| < 2.4$ and are arranged in 5 separate layers that are made up of different numbers of rings.

RPCs are made of 2 oppositely charged parallel plates that are made of a high resistivity plastic material and separated by a gaseous volume. The plates are transparent to electrons which are detected by external metallic strips. The RPCs give a coarser resolution than the DTs and CSCs, but have a timing resolution on the order of nanoseconds. They cover $|\eta| < 1.6$ and are primarily used as a secondary muon identification tool to confirm the measurements in the DTs and CSCs.

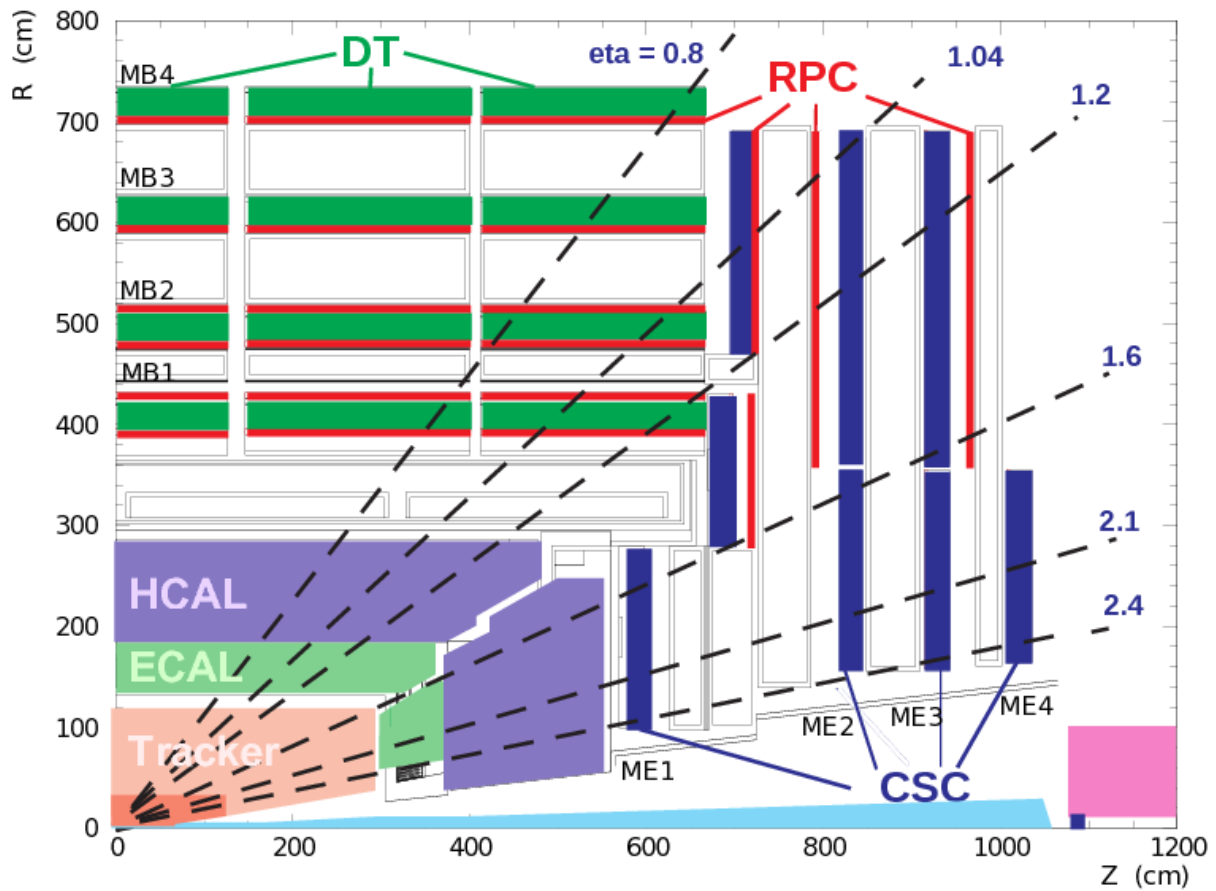


Figure 1.7: Schematic view of the muon system.

1.2.6 The Trigger System

Collisions at CMS occur every 25 ns or at a rate of 40 MHz, which is an impossible amount of data to store. To reduce the amount of data, CMS employs a trigger system that attempts to only save interesting events. To do this, the trigger system is made up of 2 triggers: the Level-1 (L1) trigger and the high level trigger (HLT). The L1 trigger consists of programmable electronics and reduces the rate to 100 kHz. The HLT uses software to reconstruct physics objects and reduces the rate to below 1 kHz.

1.2.6.1 The Level-1 Trigger

The L1 trigger uses information from every sub-detector, except for the tracker, to determine whether an event is passed to the HLT. It has a $3.2 \mu\text{s}$ latency period to make this decision and the tracker cannot provide information from its measurements in this small time frame. The final step of the L1 trigger that decides whether an event is kept or rejected is the Global Trigger and it uses information from the calorimeter trigger and muon trigger to make this decision.

The initial step of the calorimeter trigger are the Trigger Primitive Generators (TPG), which sum the transverse energies measured in ECAL crystals or HCAL read-out towers. This info is used to determine possible electrons or photons, transverse energy sums, and tau-veto bits by the Regional Calorimeter Trigger. The Global Calorimeter Trigger then determines the highest-rank calorimeter trigger objects across the entire detector. It determines jets, total transverse energy, MET, jet counts, HT, and the highest-rank isolated and non-isolated electron and photon candidates.

The muon trigger uses track segments combined from the DTs and CSCs, as well as separate track candidates from the RPCs. The Global Muon Trigger combines this information to achieve the best momentum resolution and efficiency possible and determine the four best muon candidates.

The architecture of the L1 trigger system can be seen in Figure 1.8.

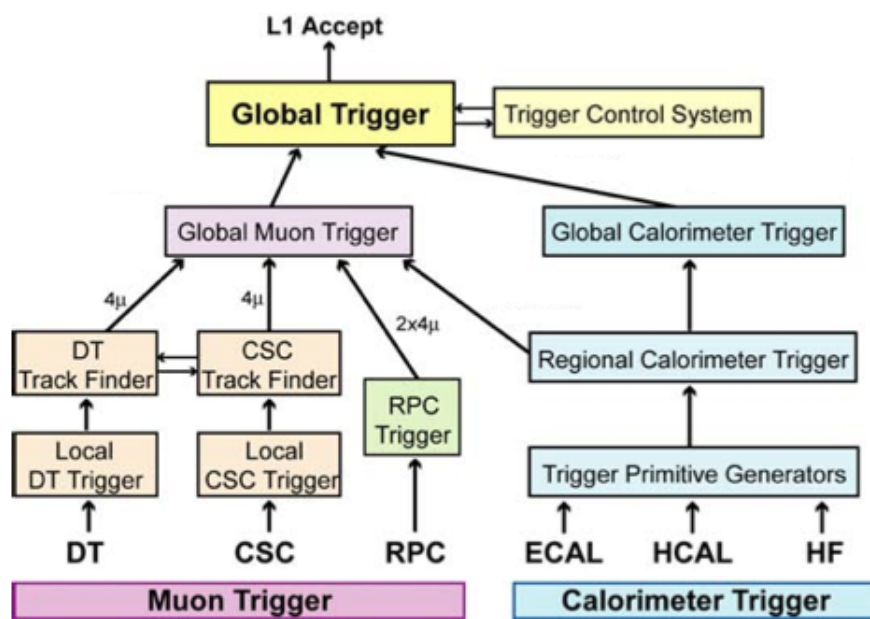


Figure 1.8: Schematic of the Level-1 trigger system.

1.2.6.2 The High Level Trigger

The HLT is a software based system that uses reconstructed physics objects to make complicated calculations. These calculations are done using similar software to what is used in offline analyses. The HLT is made up of many different HLT paths that are implemented for specific analyses and each consist of a sequence of steps of reconstructing and filtering in increasing complexity.

Chapter 2

Object Reconstruction

The CMS detector attempts to identify all particles produced in proton-proton collisions. However, all the data from an event is provided as hit patterns in the subdetectors and to simplify the analysis of these hit patterns they are first converted into physics objects. This chapter will describe the process of reconstructing physics objects from the information provided by the CMS detector.

2.1 The Particle Flow Algorithm

The Particle Flow (PF) algorithm [18, 6] optimally combines information from all the subdetectors to identify and reconstruct every individual particle produced in a proton-proton (pp) collision. To accomplish this, the CMS detector was designed with a nearly fully efficient tracking system to precisely reconstruct tracks and vertices and a calorimeter with excellent granularity to disentangle overlapping showers. The PF algorithm is comprised of three main elements: iterative tracking, calorimeter clustering, and the link algorithm.

2.1.1 Iterative Tracking

To reconstruct the charged particles from a pp collision, the hits in the tracker need to be converted into a collection of tracks. The tracking software used by the PF algorithm is called the Combinatorial Track Finder (CFT) [8] and it allows pattern recognition and track fitting to occur in the same framework. The CFT is run six times with the reconstruction criteria loosening for

each iteration to achieve both a high efficiency and low fake rate. Each iteration is comprised of four steps: seed generation, track finding, track fitting, and track selection.

Seed generation determines initial track trajectories from the minimum number of hits necessary to define a trajectory in a magnetic field. Five parameters are needed to define a helical trajectory and thus, either 3 hits or 2 hits and an additional constraint that the particle originates from the beam spot are used to define the seeds. These seeds are required to pass some minimum p_T threshold and must be consistent with originating from the pp interaction region. Next, the initial track trajectories are extrapolated out and at each detector layer the hit with the position that produces the smallest χ^2 to the extrapolated trajectory is added to the track. This process is repeated at each detector layer until the end of the tracker is reached. When there is no hit along the trajectory at a certain layer a “ghost” hit is added to the track. Tracks are discarded after a certain number of ghost hits are recorded. To obtain the full information of the trajectory, tracks are refitted with all hits using a Kalman filter and smoother [12]. Finally, tracks are selected if they pass a certain amount of quality requirements such as the number of layers with hits, the χ^2/ndf of the track fit, and the compatibility that the track originates from the primary vertex. This greatly reduces the number of fake tracks.

2.1.2 Calorimeter Clustering

There are four purposes to the clustering algorithm in the calorimeter: detect and measure the energy and direction of neutral particles, separate these neutral particles from energy deposits of charged ones, reconstruct and identify electrons and all accompanying Bremsstrahlung photons, and assist the energy measurement of charged hadrons when track parameters aren't accurately determined. The clustering algorithm is therefore designed for a high detection efficiency for low-energy particles and a separation of close energy deposits from the high granularity calorimeter. Clustering is performed separately in each subdetector as follows.

First, the seed for a cluster of nearby hits is identified as the hit with the maximum energy that is above a given threshold. Topological clusters are then created by adding cells that are adjacent

to the cells already in the cluster and have an energy above a given threshold. Finally, the final energy and position of the clusters is determined through an iterative expectation-maximization algorithm.

2.1.3 The Link Algorithm

The purpose of the link algorithm is to connect the different PF elements from the subdetectors to fully reconstruct a particle. The elements that can be linked are charged-particle tracks, calorimeter clusters, and muon tracks. The link algorithm creates blocks of elements which contain two or three elements.

A link between a track and a calorimeter cluster is made if the extrapolated track from the tracker lands within the cluster. Clusters from different calorimeter subdetectors are linked when the position in the more granular calorimeter is within the cluster envelope in the less granular calorimeter. And finally, links between tracker tracks and muon tracks are made when a global fit of the combined tracks returns an acceptable χ^2 .

2.1.4 Particle Identification

Each block of elements is identified as specific particles in the following way. First, muons are identified when the momentum of the combined tracks in the tracker and muon detector is within 3σ of the tracker momentum. The corresponding tracks are then removed from the block. Secondly, electrons are identified by finding tracks that fit the criteria of an electron track: short tracks that lose energy from Bremsstrahlung. These tracks are refit with a Gaussian-Sum fitter [1] to project their trajectories out to the ECAL and find an intersecting cluster. The corresponding track and ECAL cluster are then removed from the block. Thirdly, charged hadrons are identified from the remaining tracks and are associated to clusters in the HCAL if the cluster energy falls within the uncertainties of the track momentum. Finally, the remaining clusters in the HCAL and ECAL are associated with neutral hadrons and photons, respectively.

2.2 Vertex Reconstruction

Vertex reconstruction locates all of the pp interactions with an event. It consists of three steps: track selection, clustering tracks originating from the same vertex, and fitting the tracks for the position of each vertex.

Tracks are selected that are produced promptly in the primary interaction region. This is done by placing requirements on the impact parameter off the track relative to the center of the beam, the number of hits within the track, and the χ^2 of the fit trajectory. The tracks are then clustered according to their z-coordinate at their point of closest approach to the center of the beam spot. Finally, the position of each vertex is determined by fitting each cluster of tracks [8].

2.3 Jet Reconstruction

In an attempt to reconstruct the hadronization of a quark or gluon, the hadrons and non-isolated leptons of an event are clustered together to form jets. In this analysis, the “anti- k_t ” algorithm is used to create jets. This algorithm iteratively clusters particles together by defining two distance parameters

$$d_{ij} = \min(k_{ti}^{2p}, k_{tj}^{2p}) \frac{\Delta_{ij}^2}{R^2} \quad (2.1)$$

$$d_{iB} = k_{ti}^{2p} \quad (2.2)$$

where k_{ti} is the transverse momentum of particle i , $\Delta_{ij}^2 = (y_i - y_j)^2 + (\phi_i - \phi_j)^2$, y_i is the rapidity, ϕ_i is the azimuth, R is the chosen cone radius, and $p = -1$ gives the anti- k_t algorithm. The distance between particles i and j , d_{ij} , is compared to d_{iB} , the distance between particle i and the beam. If d_{ij} is smaller than d_{iB} then i and j are recombined, but if d_{ij} is larger then i is called a jet and removed from the remaining particles. This continues until all particles have been clustered into jets.

The anti- k_t algorithm clusters soft particles to hard ones, so that a jet's axis is mainly defined by its hard constituents. This is a key feature of the algorithm because the jet's axis will not dramatically change when soft radiation from pileup is removed from the event. When two hard particles are nearby, they are either clustered together or the soft particles are shared between them based on the size of the cones being reconstructed.

2.4 Missing Transverse Energy

The initial momentum of the colliding protons at CMS is unknown, however it is known that their transverse momentum is zero. Therefore, by conservation of momentum, the combined transverse momentum of all of the particles produced in the collision is zero. However, weakly interacting particles, like neutrinos, can avoid detection and cause there to be an imbalance in the transverse momentum of a collision. These signatures are predicted by many theoretical models and thus, a useful quantity in the analysis of CMS data is the missing transverse momentum:

$$\vec{E}_T = - \sum_{\text{detected particles}} \vec{p_T} \quad (2.3)$$

This quantity is referred to as MET throughout this paper.

Chapter 3

Radiation Tolerance of 65 nm CMOS Transistors

The need for extremely radiation tolerant electronics, especially in the era of High Luminosity running at the LHC (HL-LHC), is a major issue confronting high energy physics. The HL-LHC will begin running in 2025 and the expected peak luminosity is $5 \times 10^{34} \text{ cm}^{-2}\text{s}^{-1}$. At this luminosity, the particle flux near the collision vertex will be extremely high and the electronics in the pixel detector will need to be able to operate while accumulating a total ionizing dose of about 1 Grad.

To lower the material density and power dissipation in the pixel detector, the plan for the HL-LHC readout chips in the pixel detector at CMS is to upgrade from the current 130 nm complementary metal-oxide-semiconductor (CMOS) technology to 65 nm CMOS technology. Previous studies [3] showed that the properties of 65 nm CMOS technology did not dramatically change after being exposed to a total dose of 200 Mrad. However, these studies were conducted at room temperature and the pixel detector will be operated at -20°C to limit the leakage current in the silicon strip trackers. At a lower temperature, the CMOS devices will not anneal as much and the radiation damage might be greater than had been observed in room temperature exposures. Thus, it is important to characterize the response of 65 nm CMOS technology to large radiation doses while operating at -20°C .

This chapter summarizes an experiment [14] that characterized the response of 65 nm CMOS transistors to a cumulative radiation dose of 1 Grad while being held below -20°C .

3.1 Radiation Damage Mechanisms

Two types of radiation damage can occur when energetic particles pass through a semiconductor device and either electron-hole pairs (ionization damage) are created or silicon atoms are displaced from their lattice sites (displacement damage). This chapter will focus on ionization damage.

Ionization damage occurs in the insulating layers of the device, usually SiO_2 , when the electrons and holes drift to different locations where they are trapped and cause unwanted electromagnetic fields within the device. There are two locations of insulating layers within current semiconductors: the gate oxide and the shallow trench isolation (STI) oxide. A layout of a CMOS transistor can be seen in Figure 3.1[16].

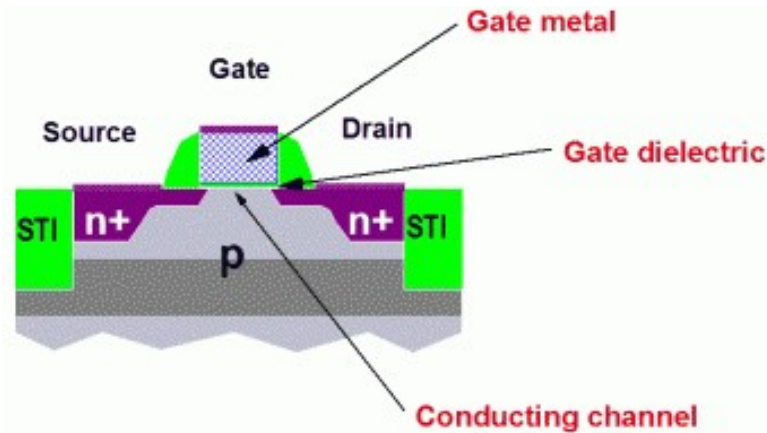


Figure 3.1: The cross section view of an n-channel transistor. The transistor is built on a p-type substrate with n-type implants as the source and drain. An inversion layer is formed in the conducting channel when a positive voltage is applied to the gate. The gate dielectric (gate oxide) and shallow trench isolation (STI) oxide are the green regions[16].

Gate oxide separates the gate terminal from the conductive channel that connects the source and drain and serves as a dielectric layer so that the gate can sustain a high electric field. When electron-hole pairs are created in the gate oxide the electrons are swept out of the oxide by the positive voltage applied on the gate terminal while holes move in the opposite direction toward the Si/SiO_2 interface. Two separate mechanisms can then occur [15]:

- **Deep Hole Trapping:** There is a transition region from SiO_2 to Si where the oxidation is not complete and there are oxygen vacancies. These vacancies cause weak Si-Si bonds, where each Si atom is also bonded to three oxygen atoms, that are broken by holes which then remain trapped there. The holes accumulate at the interface causing a buildup of positive charge.
- **Radiation-Induced Traps:** At the Si/ SiO_2 interface there are tri-valent Si atoms that have been passivated by H atoms. Radiation-induced holes free protons from the oxide and the protons then travel to the Si/ SiO_2 interface. At the interface the proton breaks the Si-H bond to form H_2 and a trivalent Si atom that is left with an unpassivated dangling bond that is an electrically active defect.

These effects cause the voltage seen by the conductive channel to differ from the actual voltage applied at the gate terminal and thus, the transistor will turn on at a different voltage than it was designed to. These mechanisms are extremely dependent on the thickness of the gate oxide and more deep hole and radiation-induced traps will build up the thicker the gate oxide is.

STI oxide is implanted in the silicon between adjacent semiconductors to prevent leakage current. The same mechanisms that occur in the gate oxide also occur in the STI oxide, however they effect the transistor functionality differently. When charge builds up in the STI oxide, a conductive channel is opened between the source and drain of the transistor and leakage current can flow even when the transistor is turned off. This is illustrated in Figure 3.2[11].

The radiation induced charge that is trapped in the STI also prevents channel inversion near the STI and reduces the conductive channel width. This is referred to as Radiation Induced Narrow Channel Effect (RINCE)[10] and is more evident in narrow channel devices. A narrower conductive channel allows less current to flow from the source to drain and thus, the maximum drain to source current that can be achieved is decreased.

Transistors can at least partially recover from these radiation induced damage mechanisms through a process called annealing. This is a complex process that occurs either when trapped

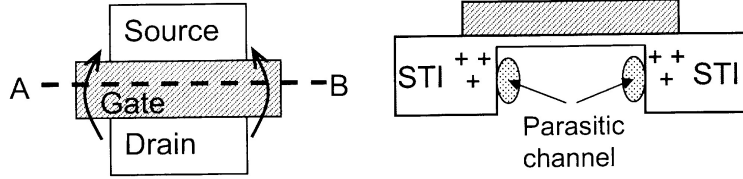


Figure 3.2: The crosses represent positive charge build up in the shallow trench isolation (STI) oxide, which allow current to pass between the source and the drain when no voltage is applied to the gate[11].

charge tunnels out of the oxide or is thermally excited enough to leave the oxide. Once a charge is free from the oxide, it is swept away by oppositely charged voltage contacts of the transistor.

3.2 Experimental Details

3.2.1 Transistor Test Setup

A 65 nm CMOS Application Specific Integrated Circuit (ASIC) containing individual transistors connected to wire bond pads was built for radiation tolerance testing. Transistors within the ASIC were laid out in groups of similar transistors, for example all N-type metal-oxide-semiconductor (NMOS) transistors with the same channel length (L). Within a group, all transistors share a gate pad and a source/drain pad. The other drain/source of the transistor is connected to its own wire bonding pad, so that each transistor characteristic can be measured individually. The devices tested were P-type metal-oxide-semiconductor (PMOS) and NMOS core transistors operated at 1.2 V and NMOS input/output (I/O) transistors with double thickness gate oxide operated at 2.5 V. Several transistor sizes were included for core PMOS and NMOS transistors: transistors with $L = 60$ nm and a channel width (W) between 120 and 1000 nm, one transistor with size $W/L = 500/500$ nm, and one with size 5000/5000 nm. Additionally, triple deep well core NMOS transistors of size 120/60 nm and 5000/60 nm were included with a zero threshold voltage 1500/300 nm transistor and a zero threshold enclosed layout (ELT) 2240/300 nm transistor. The I/O NMOS transistor sizes were $W = 280$ nm and L between 400 and 1000 nm, a transistor with size 500/500

nm, and one with size 5000/5000 nm. The following different types of I/O NMOS transistors were also included: a triple deep well 800/280 nm transistor, an ELT 2220/280 nm transistor, a zero threshold 3380/1200 nm transistor, and a zero threshold ELT 3450/1200 nm transistor.

The test ASICs were wire bonded into pin grid array (PGA) chip carriers so that they could be irradiated on simple printed circuit boards (PCBs) containing only sockets for the ASICs and connectors for bias voltage. During irradiation PMOS transistors were biased in two different ways:

- The drains, sources, and gates were held at 1.2 V and the substrate was grounded.
- The gates and substrate were grounded while the drains and sources were held at 1.2 V.

The NMOS core (I/O) transistors were biased with the gates held at 1.2 V (2.5 V) and all other nodes grounded. These are the worst-case bias conditions.

Transistor characteristics were measured by mounting a single chip carrier at a time on a different PCB test board containing switches that allow individual transistors to be measured independently. The test board was connected to two source measurement units (SMUs), one to bias transistor gates and one to measure drain-source currents. Characteristics were made by holding the core (I/O) transistors drain-source voltage at 1.2 V (2.5 V) and the drain-source current was measured as the gate-source voltage was swept from 0 to 1.2 V (2.5 V).

3.2.2 Irradiation Setup

The irradiation of the test devices was performed at the Gamma Irradiation Facility (GIF) at Sandia National Laboratories. The GIF uses ^{60}Co sources to provide controlled doses of ionizing radiation. ^{60}Co decays by beta decay to an excited state of ^{60}Ni which then relaxes to the ground state by emitting two gamma rays of energy 1.17 and 1.33 MeV. The ^{60}Co is held in stainless steel “source pins” so that none of the beta electrons escape. 40 source pins are mounted in a straight-line array that is held at the bottom of an 18 foot deep pool of deionized water to provide shielding when not in use and raised out of the water when an irradiation takes place.

The test ASICs were held inside stainless steel thermos bottles positioned approximately two inches from the face of the array of pins. Cooling was provided by vortex tube coolers mounted in holes drilled through the plastic thermos bottle lids. Figure 3.3 shows the thermos bottle assembly. To maintain the temperature of the thermos bottles, which were heated by the gamma rays interacting with the walls of the thermos bottles, the compressed air that was input to the vortex tubes was precooled and passed through insulated copper tubes. The temperature within the thermos bottles was measured and recorded by a K-type thermocouple in each thermos bottle. Figure 3.4 shows the temperature of two thermos bottles during the irradiations.

The dose rate the test ASICs received was 1425 rad/s and was measured by an ion chamber placed inside of a thermos bottle. The uniformity of the radiation field was checked by irradiating thermoluminescent dosimeters (TLDs) taped to each of the chip carriers on the irradiation PCB. The TLDs also provided a second measurement of the dose rate.

Twelve irradiations were performed over 15 days, as shown in Table 3.1, and after each irradiation step a single characteristic curve was recorded for each transistor. All measurements were made at room temperature, but when a test ASIC wasn't being irradiated or measured they were stored at -20°C in a freezer. After the full irradiation, devices were kept at room temperature for a week and multiple characteristics were taken to characterize the annealing effects. The transistors were then held in an oven at 100°C for one week to simulate an extended annealing period and a final set of measurements was made.

3.3 Analysis

Two quantities were extracted from each transistor characteristic: the maximum drain-source current and the threshold voltage, V_{th} . The quadratic extrapolation method was used to determine the threshold voltage [17]. As shown in Figure 3.5, V_{th} is defined to be the voltage at which a line tangent to the curve $\sqrt{|I_{ds}|}$ vs V_{gs} at the point of maximum $\frac{d\sqrt{|I_{ds}|}}{dV_{gs}}$ intercepts the $I_{ds} = 0$ axis. The slope of the curve was determined by fitting it with a fifth order polynomial and differentiating the fit function.

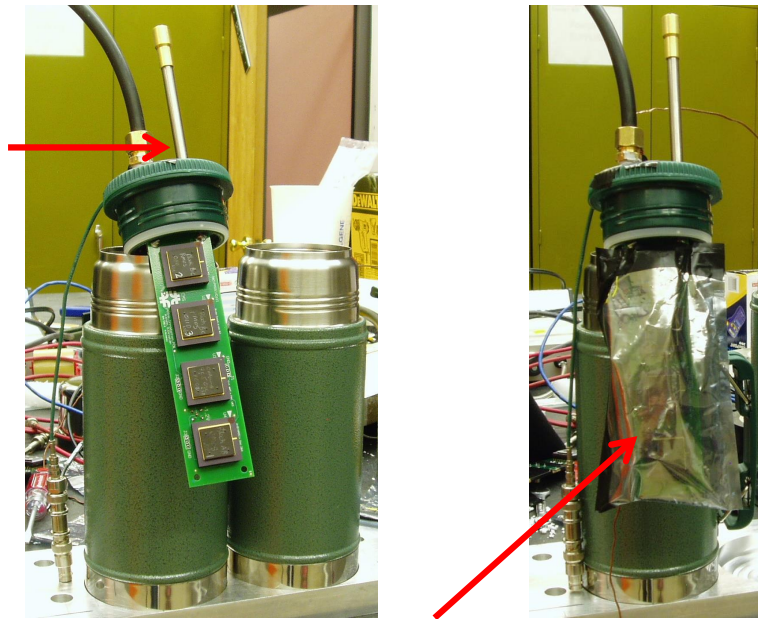


Figure 3.3: Pictures of the thermos bottle, including an irradiation printed circuit board with four chip carriers, before insertion of the irradiation board into the thermos bottle. On the left, the red arrow points to the vortex tube on top of the thermos bottle lid. On the right, the red arrow points to an antistatic bag which wraps the irradiation board and low-voltage cable before irradiation. These bags keep the boards and voltage cables dry during the irradiation.

Table 3.1: The irradiation schedule, showing the 2 weeks it took to accumulate 1 Grad.

Date	Length	Dose(Mrad)	Cumulative Dose(Mrad)
June 2	1 hour	5	5
June 3	1 hour	5	10
June 3	1 hour 45 mins	9	19
June 3	4 hour 15 mins	22	41
June 4-5	12 hours	62	103
June 5-6	22 hours	113	215
June 6-7	22 hours	113	329
June 9-10	22 hours	113	441
June 10-11	17 hours	87	528
June 11-12	22 hours	113	641
June 12-13	22 hours	113	754
June 13-16	66 hours	339	1093

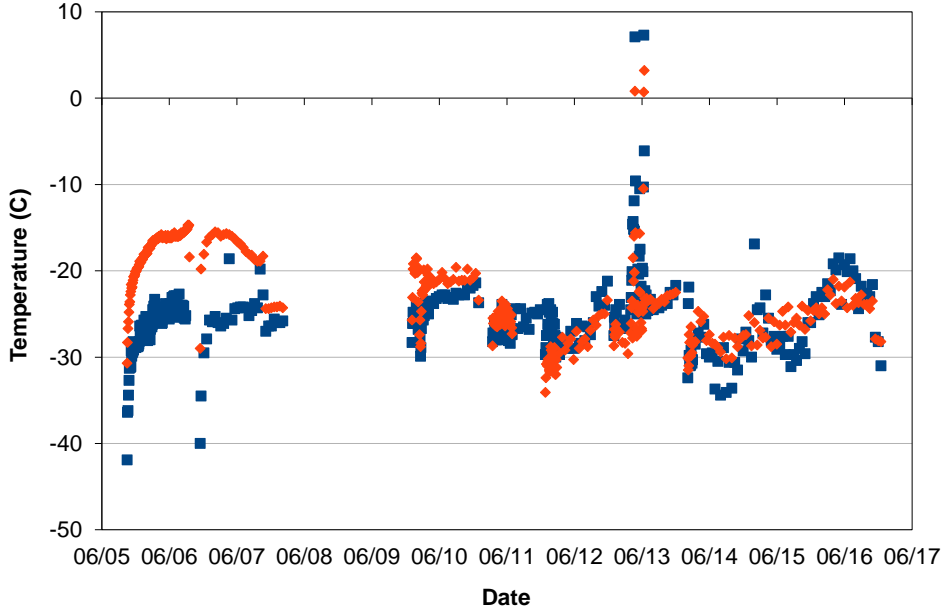


Figure 3.4: The temperature measured inside the two thermos bottles during the long irradiations. No irradiation was performed on June 8 or 9. The two spikes where the temperature reached about 8°C in both thermos bottles for 30 minutes on June 12 occurred because the compressed air unexpectedly turned off.

3.4 Results

Figure 3.6 illustrates the radiation effects observed in the data. The most prominent effect is a decrease of the maximum drain-source current of core PMOS transistors. The fractional decrease is largest for the smallest PMOS transistors and they decreased by more than a factor of two. No significant difference was observed between the radiation-induced changes of PMOS transistors held at different bias voltages. This is illustrated in Figure 3.7. The maximum drain-source current of core NMOS transistors also decreased, but only by $\sim 5 - 10\%$. No significant threshold shift was observed for any of the core transistors, but the threshold voltage of NMOS I/O transistors increased by 100 - 200 mV.

Figure 3.8 demonstrates the annealing effects observed in our data. Both the PMOS core transistors and the NMOS I/O transistors recovered significantly during the annealing period.

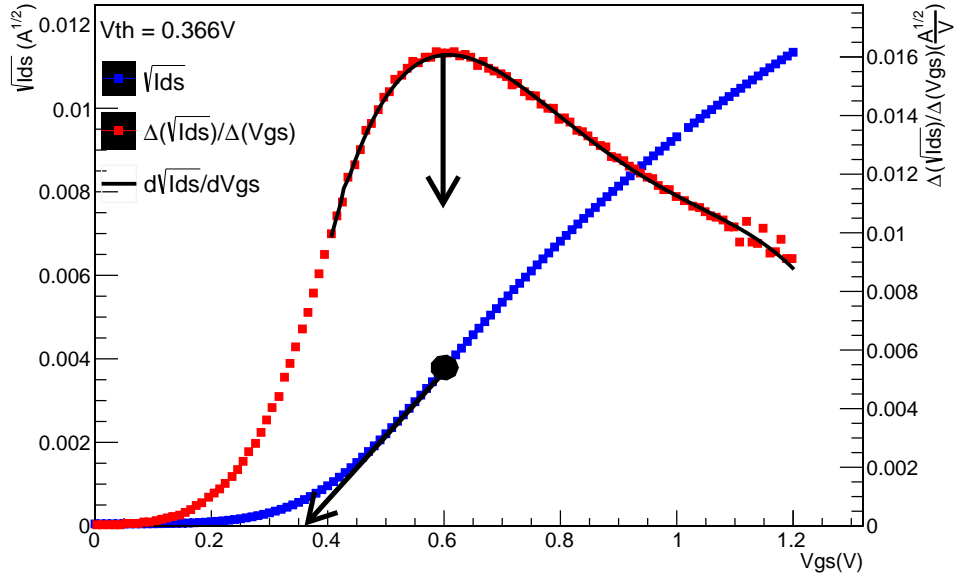


Figure 3.5: This figure illustrates the quadratic extrapolation method used to determine the threshold voltage (V_{th}) of an NMOS transistor. The blue data points are the transistor characteristic and the red ones are computed using finite differences $\frac{\sqrt{I_{ds}(N+1)} - \sqrt{I_{ds}(N)}}{V_{gs}(N+1) - V_{gs}(N)}$. The black curve is the result of differentiating the fifth order polynomial that was fit to the characteristic. V_{th} is the point on the $I_{ds} = 0$ axis where the tangent to the characteristic intersects. For PMOS transistors, $|I_{ds}|$ is used since I_{ds} is negative.

Figures 3.9 and 3.10 show the evolution of the maximum drain-source current for a representative selection of PMOS and NMOS core transistors during irradiation and annealing. There were no significant differences in the effect of radiation on the various types of NMOS transistors tested (normal layout, enclosed layout, triple well, and zero V_{th}). Figure 3.11 shows the threshold shift of a representative selection of NMOS I/O transistors during irradiation and annealing.

3.5 Summary

The irradiation of 65 nm CMOS transistors held at -20°C was motivated by the need to simulate the actual operating conditions of the HL-LHC CMS pixel detector. The results show the same pattern of effects that had been observed at room temperature irradiations except the damage observed was less severe, rather than more severe. This could be due to holes and electrons

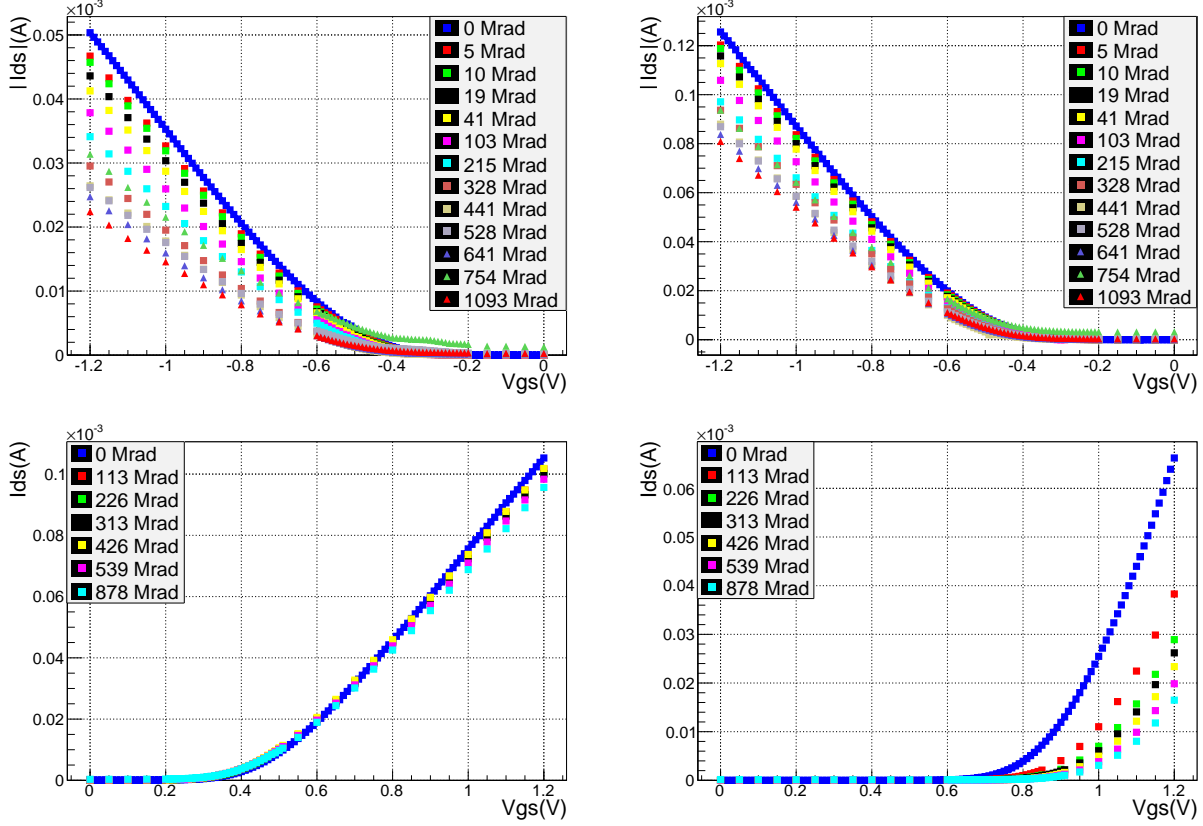


Figure 3.6: Transistor characteristic curves for total dose up to 1.1 Grad of (upper left) a 120/60 core PMOS, (upper right) a 360/60 core PMOS, and for total dose up to 878 Mrad of (lower left) a 240/60 core NMOS, and (lower right) a 1000/280 2.5 V NMOS.

traveling slower through the oxide at lower temperatures and thus, recombining more often[10].

These studies show that 65 nm CMOS transistors are a viable option for electronics within the HL-LHC CMS pixel detector.

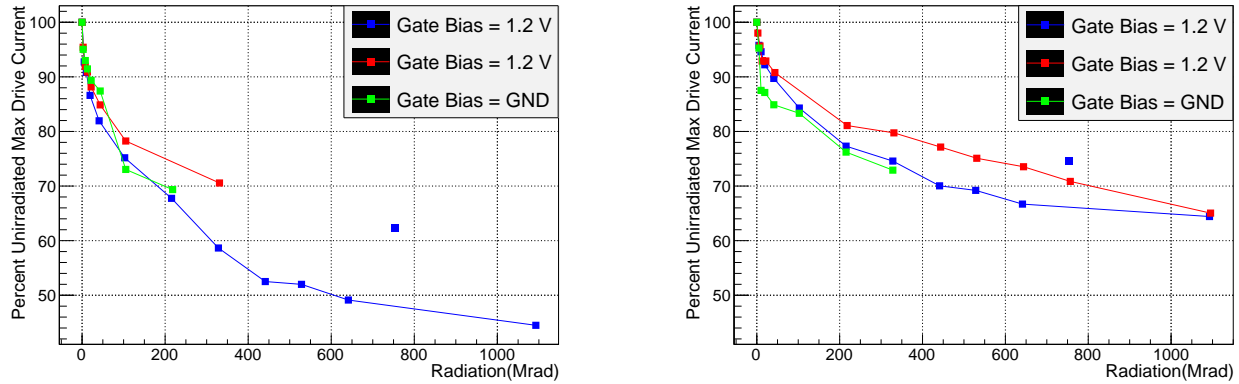


Figure 3.7: The change in maximum drain-source current for similar PMOS core transistors irradiated with different gate bias voltages. The graph on the left is for 120/60 transistors and the graph on the right is for 360/60 transistors. The lines connecting points do not represent a fit, and are included only to make the plots easier to read. The transistor characteristics measured for transistors in one of the test ASIC packages after 754 Mrad was accumulated were all offset by current not likely to have passed through the transistors (this can be seen in Figure 3.6). Lines are not drawn through these points. The most likely source of these offsets is leakage current due to moisture caused by condensation on the cold ASIC package.

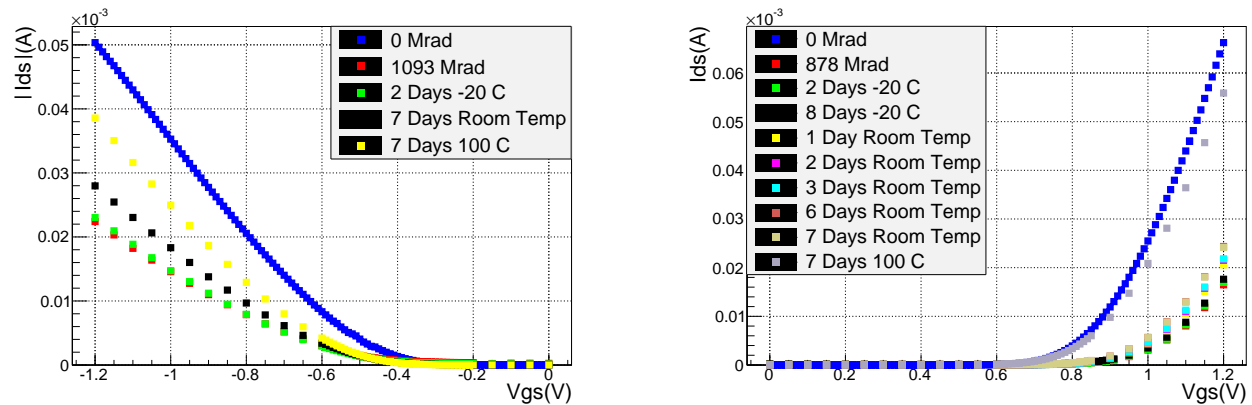


Figure 3.8: Transistor characteristic curves during the annealing period for (left) a 120/60 core PMOS and (right) a 1000/280 2.5 V NMOS.

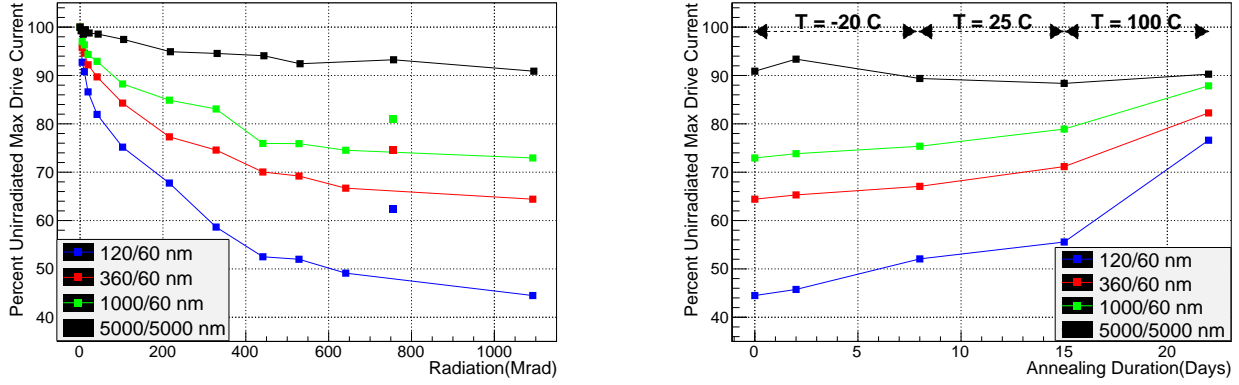


Figure 3.9: The graph on the left shows the loss of maximum drain-source current during irradiation for 4 PMOS core transistors. The graph on the right shows the recovery of maximum drain-source current for the same 4 transistors during and after annealing. As in Figure 3.11, lines are included to make the plots easier to read. Once again, lines are not drawn through the points corresponding to measurements made after 754 Mrad of transistors in one of the ASIC packages.

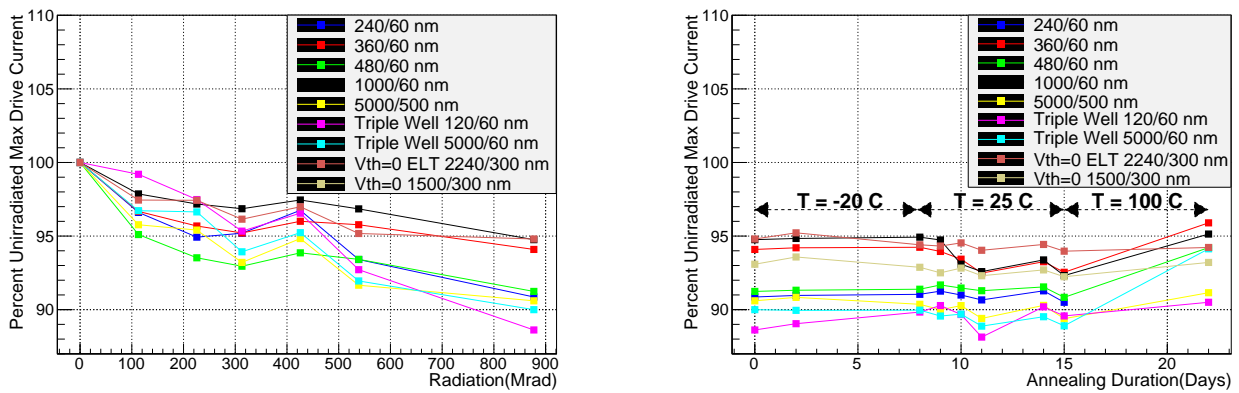


Figure 3.10: The graph on the left shows the loss in maximum drain-source current after each irradiation step for 9 NMOS core transistors. The graph on the right shows the change in maximum drain-source current for the same 9 transistors during and after annealing.

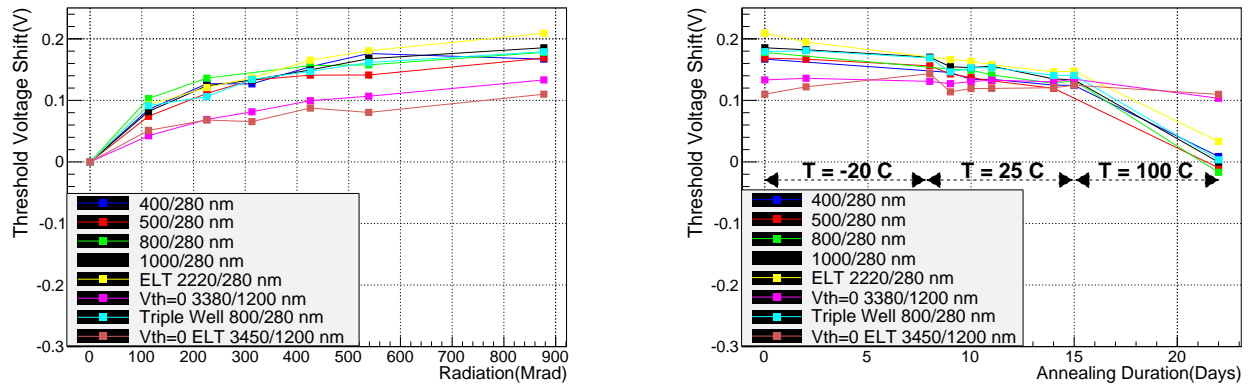


Figure 3.11: The shift in threshold voltage for 8 NMOS I/O transistors irradiated to 878 Mrad is shown in the graph on the left, while the graph on the right shows V_{th} for the same 8 transistors during and after annealing. No significant annealing was observed for the two zero V_{th} I/O transistors.

Bibliography

- [1] W. Adam, R. Fruhwirth, A. Strandlie, and T. Todorov. Reconstruction of electrons with the Gaussian-sum filter in the CMS tracker at the LHC. *Journal of Physics G: Nuclear and Particle Physics*, 31(9), 2005.
- [2] Florian Beaudette. The CMS Particle Flow Algorithm. *Proceedings of the International Conference on Calorimetry for the High Energy Frontier*, pages 295–304, 2013.
- [3] S. Bonancini, P. Valerio, R. Avramidou, R. Ballabriga, F. Faccio, K. Kloukinas, and A. Marchioro. Characterization of a commercial 65 nm CMOS technology for SLHC applications. *JINST*, 7(P01015), 2012.
- [4] CMS Collaboration. The electromagnetic Calorimeter Technical Design Report. (CERN-LHCC-97-033, CMS-TDR-4), 1997.
- [5] CMS Collaboration. The CMS experiment at the CERN LHC. *JINST*, 3(S08004), 2008.
- [6] CMS Collaboration. Particle-Flow Event Reconstruction in CMS and Performance for Jets, Taus, and E_T^{miss} . *CMS-PAS-PFT-09-001*, 2009.
- [7] CMS Collaboration. CMS Technical Design Report for the Pixel Detector Upgrade. (CERN-LHCC-2012-016), 2012.
- [8] CMS Collaboration. Description and performance of track and primary-vertex reconstruction with the CMS tracker. *JINST*, 9, 2014.
- [9] Lyndon Evans and Philip Bryant. LHC Machine. *JINST*, 3(S08001), 2008.
- [10] F. Faccio, S. Michelis, D. Cornale, A. Paccagnella, and S. Gerardin. Radiation-Induced Short Channel (RISCE) and Narrow Channel (RINCE) Effects in 65 and 130 nm MOSFETs. *IEEE Transactions on Nuclear Science*, 62(6):2933–2940, 2015.
- [11] Federico Faccio and Giovanni Cervelli. Radiation-Induced Edge Effects in Deep Submicron CMOS Transistors. *IEEE Transactions on Nuclear Science*, 52(6):2413–2420, 2005.
- [12] Rudolf Fruhwirth. Application of Kalman filtering to track and vertex fitting. *Nucl. Instrum. Meth.*, A262:444–450, 1987.
- [13] Julie Haffner. The CERN accelerator complex, 2013.

- [14] M. Krohn, B. Bentle, D.C Christian, J.P. Cumalat, G. Deptuch, F. Fahim, J. Hoff, A. Shenai, and S.R. Wagner. Radiation tolerance of 65 nm CMOS transistors. JINST, 10(P12007), 2015.
- [15] Timothy R. Oldham. Basic Mechanisms of TID and DDD Response in MOS and Bipolar Microelectronics. GSFC Radiation Effects and Analysis Group, 2011.
- [16] Phys Org. Breaking the performance barrier of 22-nm CMOS technology. <https://phys.org/news/2008-02-barrier-nm-cmos-technology.html>, 2008.
- [17] Dieter K. Schroeder. Semiconductor Material and Device Characterization. Wiley-IEEE Press, New York, 1998.
- [18] A. M. Sirunyan et al. Particle-flow reconstruction and global event description with the cms detector. JINST, 12:P10003, 2017.